

Nano-sized Mo- and Nb-doped TiO₂ as anode materials for high energy and high power hybrid Li-ion capacitors

This content has been downloaded from IOPscience. Please scroll down to see the full text.

2017 Nanotechnology 28 195403

(<http://iopscience.iop.org/0957-4484/28/19/195403>)

View [the table of contents for this issue](#), or go to the [journal homepage](#) for more

Download details:

IP Address: 128.41.61.54

This content was downloaded on 20/07/2017 at 17:50

Please note that [terms and conditions apply](#).

You may also be interested in:

[Controlled synthesis of MnO₂ nanosheets vertically covered FeCo₂O₄ nanoflakes as a binder-free electrode for a high-power and durable asymmetric supercapacitor](#)

Hongyan Gao, Junjie Xiang and Yan Cao

[One-pot synthesis of -MnS/reduced graphene oxide with enhanced performance for aqueous asymmetric supercapacitors](#)

Guanggao Zhang, Menglai Kong, Yadong Yao et al.

[Synthesis of NiMnO₃/C nano-composite electrode materials for electrochemical capacitors](#)

Pejman Kakvand, Mohammad Safi Rahmanifar, Maher F El-Kady et al.

[Morphology engineering of ZnO nanostructures for high performance supercapacitors: enhanced electrochemistry of ZnO nanocones compared to ZnO nanowires](#)

Xiaoli He, Joung Eun Yoo, Min Ho Lee et al.

[Nickel cobaltite nanosheets strongly anchored on boron and nitrogen co-doped graphene for high-performance asymmetric supercapacitors](#)

Xinyan Jiao, Xifeng Xia, Peng Liu et al.

[Development of SnS₂/RGO nanosheet composite for cost-effective aqueous hybrid supercapacitors](#)

Himani Chauhan, Manoj K Singh, Praveen Kumar et al.

[Doped graphene supercapacitors](#)

Nanjundan Ashok Kumar and Jong-Beom Baek

[Flexible supercapacitors based on low-cost tape casting of high dense carbon nanofibers](#)

Allan Daraghmeh, Shahzad Hussain, Llorenç Servera et al.

Nano-sized Mo- and Nb-doped TiO₂ as anode materials for high energy and high power hybrid Li-ion capacitors

Dustin Bauer^{1,2}, Alexander J Roberts³, Noriyoshi Matsumi² and Jawwad A Darr¹

¹ Department of Chemistry, University College London, 20 Gordon Street, London, WC1H 0AJ, United Kingdom

² School of Materials Science, Japan Advanced Institute of Science and Technology, 1-1 Asahidai, 923-1211 Nomi, Ishikawa, Japan

³ WMG, University of Warwick, CV4 7AL Coventry, United Kingdom

E-mail: j.a.darr@ucl.ac.uk

Received 21 December 2016, revised 14 March 2017

Accepted for publication 29 March 2017

Published 19 April 2017



CrossMark

Abstract

Nano-sized Mo-doped titania (Mo_{0.1}Ti_{0.9}O₂) and Nb-doped titania (Nb_{0.25}Ti_{0.75}O₂) were directly synthesized via a continuous hydrothermal flow synthesis process. Materials characterization was conducted using physical techniques such as transmission electron microscopy, powder x-ray diffraction, x-ray photoelectron spectroscopy, Brunauer–Emmett–Teller specific surface area measurements and energy dispersive x-ray spectroscopy. Hybrid Li-ion supercapacitors were made with either a Mo-doped or Nb-doped TiO₂ negative electrode material and an activated carbon (AC) positive electrode. Cells were evaluated using electrochemical testing (cyclic voltammetry, constant charge discharge cycling). The hybrid Li-ion capacitors showed good energy densities at moderate power densities. When cycled in the potential window 0.5–3.0 V, the Mo_{0.1}Ti_{0.9}O₂/AC hybrid supercapacitor showed the highest energy densities of 51 Wh kg⁻¹ at a power of 180 W kg⁻¹ with energy densities rapidly declining with increasing applied specific current. In comparison, the Nb_{0.25}Ti_{0.75}O₂/AC hybrid supercapacitor maintained its energy density of 45 Wh kg⁻¹ at 180 W kg⁻¹ better, showing 36 Wh kg⁻¹ at 3200 W kg⁻¹, which is a very promising mix of high energy and power densities. Reducing the voltage window to the range 1.0–3.0 V led to an increase in power density, with the Mo_{0.1}Ti_{0.9}O₂/AC hybrid supercapacitor giving energy densities of 12 Wh kg⁻¹ and 2.5 Wh kg⁻¹ at power densities of 6700 W kg⁻¹ and 14 000 W kg⁻¹, respectively.


Supplementary material for this article is available [online](#)

Keywords: continuous hydrothermal flow synthesis, doped anatase, hybrid Li-ion capacitor

(Some figures may appear in colour only in the online journal)

1. Introduction

A worldwide increase in energy demand, and concerns over air pollution and global warming, have led to the widespread application of renewable energy sources as well as to an exploration for better energy storage systems. (Hybrid) electric vehicles are becoming more common and could play an important role both for the reduction of air pollution in cities

 Original content from this work may be used under the terms of the [Creative Commons Attribution 3.0 licence](#). Any further distribution of this work must maintain attribution to the author(s) and the title of the work, journal citation and DOI.

and for the move away from fossil fuels. Li-ion batteries have dominated in the drive towards personal electronics and electric vehicles (Palaci n 2009). Whilst Li-ion batteries benefit from low self-discharge and high energy density, supercapacitors utilizing electrochemical double layer capacitance (EDLC) show more promise for applications with a higher power demand such as regenerative braking in hybrid electric vehicles (Ibrahim *et al* 2008, Li *et al* 2016). However, EDLCs suffer from significantly reduced energy densities (Hu *et al* 2015), unless the specific surface area of the active carbon is sufficiently high to allow high energy and power densities simultaneously (Lust *et al* 2002, Stoller *et al* 2011, H rmas *et al* 2016). This problem can be addressed by developing battery-supercapacitor hybrid devices (Li *et al* 2015, Zuo *et al* 2017). Hybrid Li-ion capacitors employ a high energy battery electrode in combination with an EDLC electrode in an organic electrolyte (Plitz *et al* 2006). This approach allows for improved energy density as a consequence of fast Faradaic redox reactions on or near the surface of the battery electrode and the large potential window due to the organic electrolyte (Deng *et al* 2014).

Various materials have previously been used as negative electrode and positive electrode in combination with activated carbon (AC), including $\text{Li}_4\text{Ti}_5\text{O}_{12}$ (Naoi *et al* 2010), LiCrTiO_4 (Aravindan *et al* 2014), VO_2 (Xia *et al* 2015), porous TiO_2 (Brezesinski *et al* 2009) and anatase TiO_2 -reduced graphene oxide composites (Kim *et al* 2013). Other Li-ion hybrid capacitors have used CNT cathodes with $\text{Li}_4\text{Ti}_5\text{O}_{12}$ (Zuo *et al* 2015) or TiO_2 microspheres wrapped with graphene nanosheets versus a graphene nanosheet positive electrode (Wang *et al* 2016).

Nano-sized TiO_2 is a very promising material for use in anodes in hybrid supercapacitors because of its favourable redox potential (Aravindan *et al* 2014) of ca. 1.8 V versus Li/Li^+ (Yang *et al* 2009), which allows for a convenient voltage window when using an AC cathode, which lies within the stable potential window of liquid electrolytes. Some of its polymorphs (including anatase (Wang *et al* 2007), Nb-doped anatase (L bke *et al* 2015), $\text{TiO}_2(\text{B})$ (Dylla *et al* 2013), and TiO_2 bronze (Liu *et al* 2011)) have been shown to exhibit pseudocapacitive charge storage behaviour. It is important, however, to consider the imbalances in energy and power densities between the Faradaic charge storage in the battery-like electrode and the non-Faradaic charge storage on the surface of the AC electrode. In particular, the much slower charge storage due to intercalation into the bulk of many insertion type materials has been a limiting factor in high power applications (Kim *et al* 2013). The much faster nature of the surface or near-surface reversible redox reactions associated with pseudocapacitance on the other hand, allows for higher charge storage for significantly faster charge/discharge regimes (Augustyn *et al* 2014).

Herein, the authors demonstrate, for the first time, that doped anatase nanomaterials such as $\text{Mo}_{0.1}\text{Ti}_{0.9}\text{O}_2$ or $\text{Nb}_{0.25}\text{Ti}_{0.75}\text{O}_2$ synthesised via a continuous hydrothermal flow method can be incorporated into hybrid supercapacitors with an AC cathode to show high energy densities at high power densities.

2. Experimental section

2.1. Materials

The precursors used were TiBALD (Titanium(IV) bis (ammonium lactato)dihydroxide solution, 50 wt% in H_2O , Sigma Aldrich, Dorset, UK), 99.98% ammonium molybdate tetrahydrate (Sigma Aldrich, Dorset, UK), >99.99% ammonium niobate(V) oxalate hydrate (Sigma Aldrich, Dorset, UK) and KOH (Fisher Scientific, Loughborough, UK). The syntheses of both nano- TiO_2 and $\text{Nb}_{0.25}\text{Ti}_{0.75}\text{O}_2$ have been described in the literature previously (L bke *et al* 2015).

2.2. Synthesis

TiO_2 , $\text{Mo}_{0.1}\text{Ti}_{0.9}\text{O}_2$ and $\text{Nb}_{0.25}\text{Ti}_{0.75}\text{O}_2$ nanomaterials were synthesized using a laboratory scale continuous hydrothermal flow synthesis (CHFS) reactor that was similar to processes previously described in the literature, at the pilot (Gruar *et al* 2013) and lab (Chen *et al* 2011) scales. The rate of production was calculated to be ca. 75 g per hour. However, the pilot scale equivalent process can manufacture >2 kg of the materials per hour. The CHFS process of the authors on all scales employed a patented co-current confined jet mixer (CJM, US Patent No. 20130136687), made from standard SwagelokTM parts (Swagelok Company, Hertfordshire, UK) that allow efficient mixing of the supercritical water stream with the ambient temperature aqueous metal salt solution stream. The CJM used herein has previously been described elsewhere (Gruar *et al* 2013, Tighe *et al* 2013). In the CHFS process, three diaphragm pumps were pressurized to 24.1 MPa and used to supply the three liquid feeds. Pump 1 supplied DI water (10 M Ω) at a flow rate of 80 ml min⁻¹, which was heated in flow to 450 °C (or 400 °C for undoped titania) using a 7 kW customized electrical water heat-exchanger (that is above the critical point of water of $T_c = 374$ °C and $P_c = 22.1$ MPa). Pump 2 supplied the ambient temperature metal salt precursor mixture at a flow rate of 40 ml min⁻¹ and Pump 3 supplied 0.3 M KOH (or DI water for the synthesis of undoped titania) at a flow rate of 40 ml min⁻¹. The feeds from pump 2 and 3 were first combined in flow in a dead-volume tee-piece at room temperature, before they were mixed with the supercritical water flow to give a reactor mixing temperature of 335 °C (or 305 °C in the case of undoped titania) with a residence time of ca. 5 s.

Full details of the synthesis conditions including the concentrations of reagents used are given in the supplementary information (table S1 is available online at stacks.iop.org/NANO/28/195403/mmedia). After nucleation of the nanoparticles in the mixer, a pipe-in-pipe heat exchanger (1 m in length) was used in the CHFS process to cool the temperature of the product stream to ca. 40 °C, after which the nanoparticles exited the reactor via a back-pressure regulator valve. The particles were then collected and cleaned by dialysis in DI water for 48 h before being freeze-dried (Virtis Genesis 35XL, Biopharma process systems, Winchester, UK) via first cooling to -40 °C under vacuum of 13.3 Pa and subsequent heating to room temperature over the course of

22 h under vacuum. The as-synthesised, freeze-dried powders were used to make printed anodes without any further treatment whatsoever.

2.3. Physical characterization

Powder x-ray diffraction (PXRD) was performed to collect diffraction patterns in a 2θ range of 2° – 40° , with a step size of 0.5° , and a step time of 20 s on a STOE StadiP diffractometer (STOE, Darmstadt, Germany) using Mo-K α radiation ($\lambda = 0.71 \text{ \AA}$).

High-resolution transmission electron microscopy (TEM) using a Jeol JEM 2100—LaB $_6$ filament (Joel, Hertfordshire, UK) was used to determine size, interlayer spacing and particle morphology. A Gatan Orius digital camera was used for image capture of the samples that were pipetted on a 300 mesh copper film grid (Agar Scientific, Stansted, UK). Energy dispersive x-ray spectroscopy (EDX) also used the Jeol JEM 2100 for elemental analysis of the samples.

The valence states of the metal ions were determined using x-ray photoelectron spectroscopy (XPS) collected on a Thermo Scientific K-alphaTM spectrometer using Al-K α radiation equipped with a 128-channel position sensitive detector. High-resolution regional scans for the elements were conducted at 50 eV. Processing of the XPS data was performed using CasaXPSTM software (version 2.3.16) and by calibrating the spectra using the C 1s peak at 284.8 eV.

Brunauer–Emmett–Teller (BET) surface area measurements were carried out using liquid N $_2$ in a Micrometrics Tristar II (Micrometrics UK Ltd, Hertfordshire, UK). The samples were degassed at 150 °C (12 h) using Ar gas before measurements were undertaken.

The tap density of the synthesised nanopowders was estimated by filling the powder (2 g) into a graduated measuring cylinder (10 ml), followed by tapping it vertically on the bench 300 times by hand.

2.4. Electrochemical characterization

The negative electrodes were prepared by mixing of the active material (doped or undoped TiO $_2$) with binder (polyvinylidene fluoride, PVDF, PI-KEM, Staffordshire, UK) and conductive carbon black (Super P, Alfa Aesar, Heysham, UK) in a ratio of 80:10:10 wt%. A 10 wt% solution of PVDF in N-Methyl-2-pyrrolidone, NMP (Sigma Aldrich, Dorset, UK) was prepared using a magnetic stirrer and then mixed by hand with the conductive carbon and the active material and further NMP (ca. 2.5 ml) was added to give a viscous slurry. The slurry was ball-milled at 800 rpm for 1 h before being cast on 9 μm thick copper foil (PI-KEM, Staffordshire, UK). The electrode sheets were dried on a hotplate at ca. 150 °C for 20 min. The active mass loading of the anodes was in the range 1.2–1.5 mg cm $^{-2}$.

Positive electrodes were prepared by mixing AC active material (YP50F, Kuraray Chemical Co., Osaka, Japan) with binder (PVdF, 8 wt% solution in NMP) and carbon black (Super P) in a Buhler high torque mixer for several hours. The mass ratio of active material to binder to carbon was 87:8:5.

The resulting ink was then coated on a Megtec reel-to-reel coater in comma bar setup before passing through a three-phase oven for drying. Residual solvent and any water were then removed by further drying under vacuum at 120 °C for 12 h. The mass loading of the final positive electrodes was 5 mg cm $^{-2}$.

The initial half-cell testing of the individual electrodes using the different TiO $_2$ active materials, or AC, were performed in CR2032 coin cells using galvanostatic charge/discharge measurements and potentiodynamic cyclic voltammetry (CV) in half-cells against lithium. All the full-cell testing of the hybrid supercapacitors, using an anode with doped or undoped TiO $_2$ as active material and an AC positive electrode, was carried out in two-electrode Swagelok-type cells. All cells were assembled in an Ar-filled glovebox with O $_2$ and H $_2$ O limited below 3 ppm. Whatman (Buckinghamshire, UK) GF/B glass microfiber filters were used as separators and drenched in electrolyte of 1 M LiPF $_6$ in 3:7 wt% ethylene carbonate/ethyl methyl carbonate (BASF, Ludwigshafen, Germany). For half-cells, lithium metal foil (PI-KEM, Staffordshire, UK) was used as counter electrode, whereas in the full cells, the doped or undoped TiO $_2$ electrodes were used as the anode and the AC electrodes were used as cathodes. The half-cell constant charge/discharge (CCD) cycling was carried out on an Arbin Instrument Model BT-2000 battery tester (Caltest Instruments, Guildford, UK) at room temperature of ca. 20 °C. For the TiO $_2$ electrodes, tests were carried out in the range 1.0–3.0 V versus Li/Li $^+$ at specific currents in the range 0.1–15 A g $^{-1}$. The AC electrodes were tested in the range 3.0–4.2 V versus Li/Li $^+$ at specific currents in the range 0.1–0.5 A g $^{-1}$. CV for the half-cells were recorded in potential windows of 1.0–3.0 V versus Li/Li $^+$ for the TiO $_2$ electrodes and 3.0–4.2 V versus Li/Li $^+$ for the AC cathodes, at scan rates in the range 0.05–50 mV s $^{-1}$.

CCDs and CVs of the hybrid supercapacitors were performed on a Gamry Interface 1000 (Scientific & Medical Products Ltd, Cheshire, UK). The CVs were performed at scan rates in the range 5–100 mV s $^{-1}$ in the potential windows of 0.5–3.0 V and 1.0–3.0 V, respectively. CCDs were performed at current densities in the range 0.5–20 mA cm $^{-2}$ (relative to the area of the anode, equivalent to specific currents of ca 0.1–4.0 A g $^{-1}$ based on the mass of active material in both anode and cathode) in the potential windows of 0.5–3.0 V and 1.0–3.0 V, respectively.

3. Results and discussion

The dried nanoparticles were obtained with yields of >90% for undoped TiO $_2$, Mo $_{0.1}$ Ti $_{0.9}$ O $_2$ and Nb $_{0.25}$ Ti $_{0.75}$ O $_2$.

The PXRD patterns for the as-prepared powders revealed broad, but distinctive peaks for all samples (see figure 1). The peaks were in good agreement with JCPDS reference card no. 071-1167, corresponding to anatase TiO $_2$ (space group $I4_1/amd$). Neither of the doped samples showed any additional peaks, which suggested the Mo- and Nb-ions were doped into the anatase crystal structure.

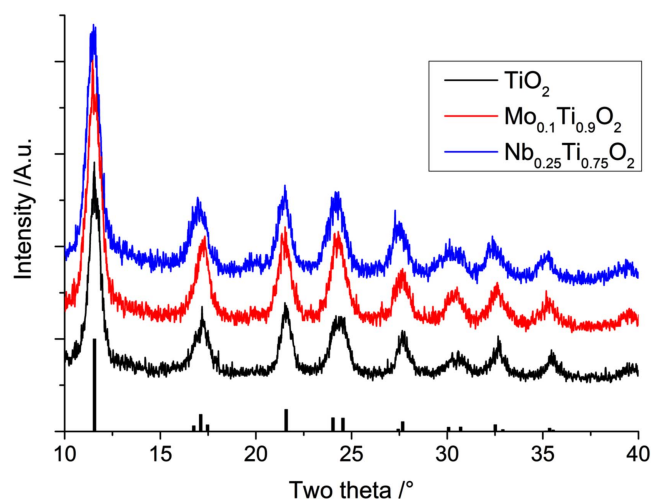


Figure 1. XRD pattern of the three synthesised samples, with the reference pattern for JCPDS card no. 071-1167 for comparison.

A closer analysis of the PXRD peaks indicated a minor shift of the peaks to lower two theta values at high angles for both the Mo- and Nb-doped TiO₂ samples. This shift was more pronounced for Nb_{0.25}Ti_{0.75}O₂ than it was for Mo_{0.1}Ti_{0.9}O₂; the shifts were presumed to be due to homogeneous doping of slightly larger ions [(Nb⁵⁺ (0.64 Å) and Mo⁶⁺ ions (0.62 Å)] into the anatase structure, replacing Ti⁴⁺ ions (0.61 Å). This observation was in good agreement with previous reports for both Nb-doped TiO₂ (Lübke *et al* 2015) and Mo-doped TiO₂ (Zhang *et al* 2014). Scherrer analysis of the PXRD patterns, suggested estimated crystallite sizes of *ca.* 6 nm for all samples. The BET surface area for the Mo_{0.1}Ti_{0.9}O₂ was 236 m² g⁻¹, which was similar to the value of 239 m² g⁻¹ previously reported for the Nb_{0.25}Ti_{0.75}O₂ sample.

TEM revealed similar particle sizes and shapes for both the undoped and doped samples. TEM images suggested an average particle size of 4.6 ± 1.1 nm for Mo_{0.1}Ti_{0.9}O₂ (100 particles counted), which was comparable to the 4.5 and 4.9 nm for undoped TiO₂ and Nb_{0.25}Ti_{0.75}O₂, respectively, that were previously reported (Lübke *et al* 2015). The inter-layer spacing was determined as 0.34 nm for the Mo-doped sample, which is consistent with previous findings and corresponded to the (101) interplanar spacing of anatase (see figure 2).

EDX analysis revealed an even distribution of molybdenum ions throughout the Mo_{0.1}Ti_{0.9}O₂ particles as expected (see figure 2(b)). This homogeneity has been previously observed for the Nb-doped sample (Lübke *et al* 2015). The mass percentage of Ti and Mo-ions were compared and the atom percentage of each calculated using the respective atomic mass. This analysis was in good agreement with the original Ti:Mo molar ratio used in the synthesis, suggesting a value of 10 ± 0.5 at% Mo in the structure with respect to Ti.

To determine the valence state of the metal ions in both the doped samples as well as the undoped TiO₂, high-resolution XPS was performed. The Ti 2p level binding energies

were very similar for all samples, with peaks at 459.2 and 465.0 eV for Ti 2p_{3/2} and Ti 2p_{1/2}, respectively (see figure S1). This gives a spin-orbit splitting of 5.8 eV and can be ascribed to the core level of Ti⁴⁺. For Mo_{0.1}Ti_{0.9}O₂, a high resolution study of the Mo 3d level showed peaks at 233.2 and 236.3 eV, associated with the core levels of Mo⁶⁺ of Mo 3d_{3/2} and Mo 3d_{5/2}, respectively, with a spin-orbit splitting of 3.1 eV (Ji *et al* 2014). Because of the lack of any additional peaks in the high-resolution spectra, it was expected that the only Ti species present in the samples was Ti⁴⁺ and the only Mo species present in Mo_{0.1}Ti_{0.9}O₂ was Mo⁶⁺. It should be remembered that XPS is only a surface technique and therefore only gave an indication of valence state of near-surface ions. It has previously been suggested that the Mo⁶⁺ doping in Ti⁴⁺ sites leads to Ti⁴⁺ vacancies in the TiO₆ octahedra (Thi *et al* 2014). A semi-quantitative analysis of the peak areas for the Mo-doped sample suggested an estimated elemental composition of *ca.* 11 at% molybdenum, which was similar to the 1:9 atom ratio for Mo:Ti that was used in the synthesis.

The tap density of the undoped TiO₂ powder was 1.17 g cm⁻³, which increased for both doped samples to high values of 1.32 and 1.27 g cm⁻³ for Mo_{0.1}Ti_{0.9}O₂ and Nb_{0.25}Ti_{0.75}O₂, respectively.

The electrochemical performance of the individual electrodes, including the AC cathodes, was evaluated before construction of full cells, using cyclic charge discharge and CV. The various titania based electrodes were studied in the potential window of 1.0–3.0 V versus Li/Li⁺, whereas the AC carbon electrode was tested in the potential window 3.0–4.2 V versus Li/Li⁺. The specific capacities at various current rates for all samples are shown in figure 3.

At a specific current of 0.5 A g⁻¹, the specific capacities were *ca.* 45, 155, 170 and 160 mAh g⁻¹ for the AC, undoped TiO₂, Mo_{0.1}Ti_{0.9}O₂ and Nb_{0.25}Ti_{0.75}O₂ electrodes, respectively. At higher specific currents, Mo_{0.1}Ti_{0.9}O₂ showed significantly higher specific discharge capacities than undoped TiO₂ of *ca.* 100 and 65 mAh g⁻¹ compared to 75 and 45 mAh g⁻¹, respectively, at 5 and 10 A g⁻¹, respectively. At the highest specific current of 15 A g⁻¹ (equivalent to a C-rate of *ca.* 45), the specific capacities for Mo_{0.1}Ti_{0.9}O₂ and TiO₂ were 42 and 25 mAh g⁻¹, respectively, which showed that molybdenum doped anatase had significantly better high rate performance than TiO₂, but slightly worse performance than previously reported Nb_{0.25}Ti_{0.75}O₂ (Lübke *et al* 2015).

To make charge stored in electrodes between samples comparable, an active mass ratio for anode and cathode of *ca.* 2:7 was used (see ESI). The CVs of the electrodes in half-cells versus Li/Li⁺ were also studied. The AC electrodes showed a nearly rectangular profile as expected for double layer-type electrodes, whilst Mo-doped TiO₂ electrodes showed clear peaks at the expected potentials versus Li/Li⁺ that are generally associated with redox reactions with Li⁺ ions (figure 4(a)); the redox peaks were observed at 1.85 and 1.60 V versus Li/Li⁺ at a scan rate of 0.05 mV s⁻¹. Because all the synthesised anode materials had an average particle size in the range 4–6 nm, which resulted in high surface areas, (extrinsic) pseudocapacitive contributions were expected to play a significant role herein. This has previously been

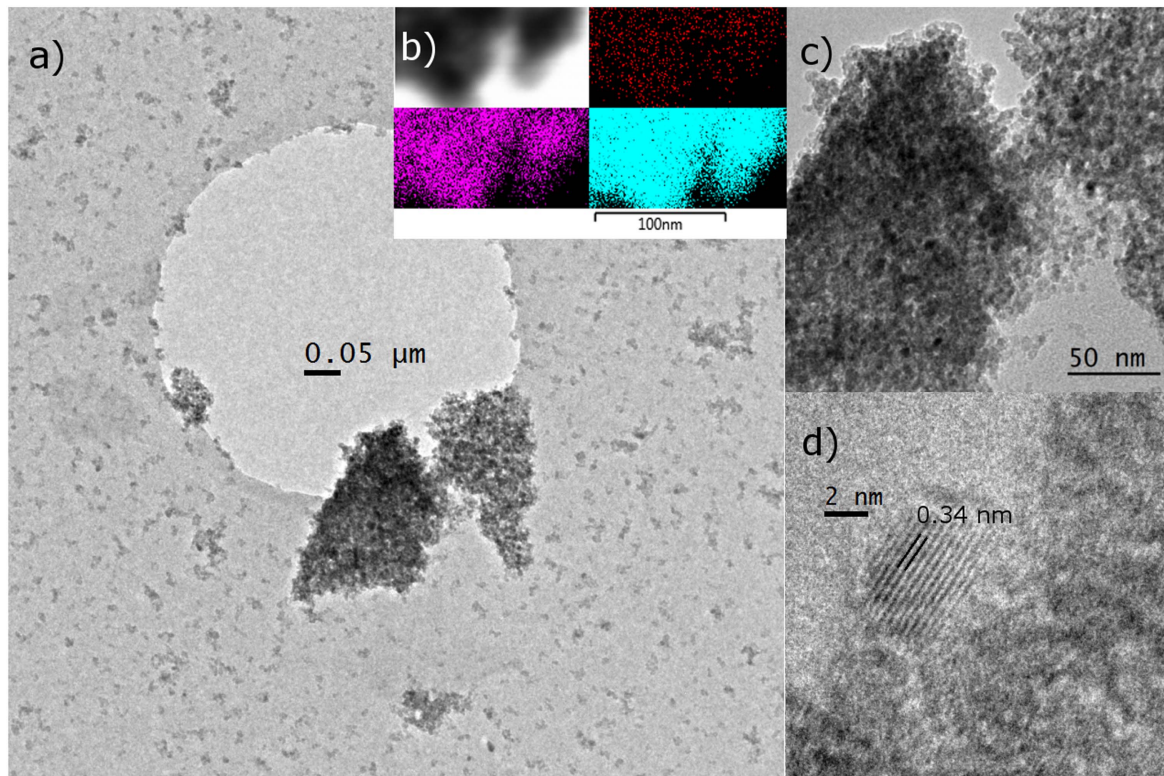


Figure 2. Transmission electron microscopy (TEM) images of the as synthesised $\text{Mo}_{0.1}\text{Ti}_{0.9}\text{O}_2$, showing an overview of particles and their agglomeration (a), a detailed agglomerate (c) and inter-lattice spacing (d) for anatase TiO_2 . Energy dispersive x-ray spectroscopy (EDX) results showing homogenous distribution of Mo (red), Ti (red) and O (blue) are also shown.

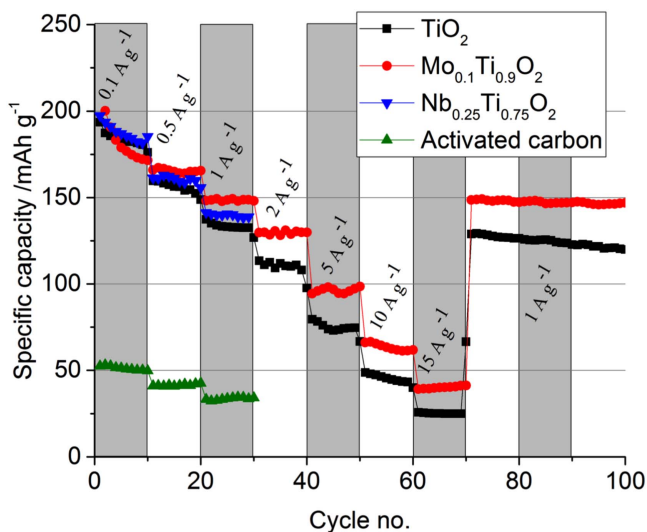


Figure 3. Half-cell data for the doped titania samples and the activated carbon electrodes.

reported for anodes in Li-ion batteries using nanosized TiO_2 (anatase) (Wang *et al* 2007), Nb-doped TiO_2 (Lübke *et al* 2015) and potentially Mo-doped TiO_2 (Thi *et al* 2014).

The CVs of the full-cell, hybrid Li-ion supercapacitors showed profiles that resembled a mixture of the individual electrode profiles. For the hybrid supercapacitors, there were clear peaks indicating partial redox reactions on the insertion-type anode, and double layer contributions from

the EDLC-type AC electrode (see figure 4(b)), as previously observed for similar devices in the literature (Kim *et al* 2013, Lee *et al* 2014, Lim *et al* 2014, Lee *et al* 2015). The anodic and cathodic redox peaks were observed at ca. 2.35 and 2.15 V, respectively, for all studied supercapacitors at the scan rate of 5 mV s^{-1} . The CV data for all supercapacitors was also used to calculate the specific capacitance of the devices (C_{cell}) at different scan rates using equation (1):

$$C_{\text{cell}} = q / (\Delta V * m), \quad (1)$$

where q is the charge in Coulombs, ΔV is the voltage change in V and m is the mass of active material in both the anode and cathode in g. In the wider potential window range of 0.5–3.0 V, Mo-doped TiO_2 showed the highest capacitance of 53 F g^{-1} (corresponding to a specific capacity of 37 mAh g^{-1}) at a scan rate of 5 mV s^{-1} , whilst Nb-doped TiO_2 could retain much of its initial specific capacitance of 47 F g^{-1} (corresponding to a specific capacity of 33 mAh g^{-1}) at 5 mV s^{-1} as well as a value of 37 F g^{-1} (corresponding to 26 mAh g^{-1}) at 100 mV s^{-1} .

This can be explained by additional charge storage in the range 0.5–1.0 V at higher scan rates for the Nb-doped TiO_2 , see comparison between the three different hybrid supercapacitors at 10 and 100 mV s^{-1} (figures 5(a) and (b)). In the narrower potential window, charge storage for the Mo-doped TiO_2 remained nearly the same and appeared much less dependent on scan rate (figures 5(c) and (d)). In the narrower potential window of 1.0–3.0 V, the hybrid supercapacitor

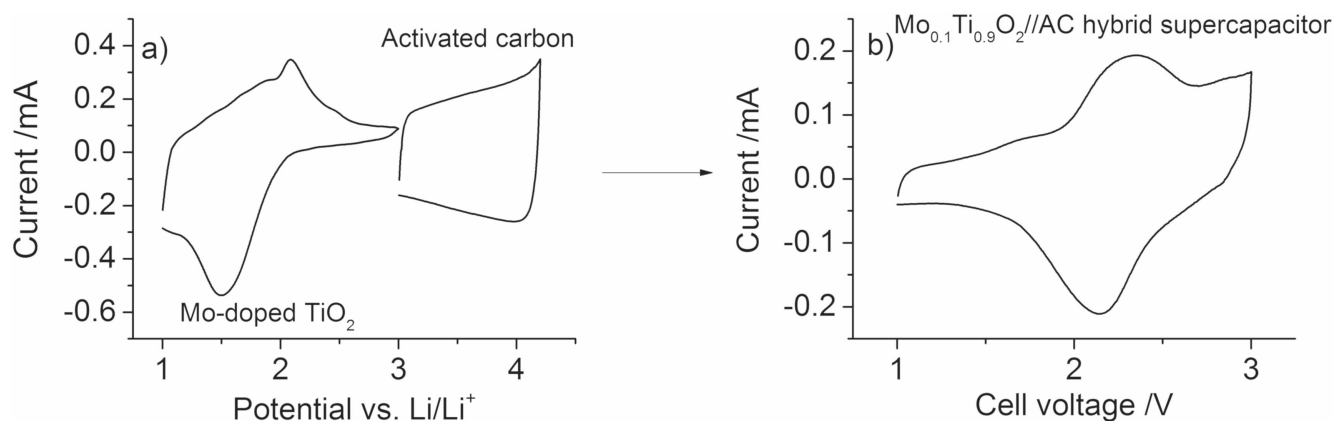


Figure 4. (a) Cyclic voltammetry (CV) data for the Mo-doped TiO_2 and the AC in half-cells at 0.5 mV s^{-1} when tested versus Li metal and (b) the CV for the Mo-doped TiO_2 /AC hybrid supercapacitor at 1 mV s^{-1} .

with the $\text{Mo}_{0.1}\text{Ti}_{0.9}\text{O}_2$ electrode still showed the highest specific cell capacitance of 56 F g^{-1} at 5 mV s^{-1} (corresponding to 31 mAh g^{-1}) and capacitance retention at higher scan rates appeared to be significantly improved. This can be explained by the fact that there is hardly any charge storage observed in the range $0.5\text{--}1.0 \text{ V}$ at higher scan rates for the $\text{Mo}_{0.1}\text{Ti}_{0.9}\text{O}_2$ /AC hybrid supercapacitor, and the charge storage in the potential window $1.0\text{--}3.0 \text{ V}$ was more reliant on pseudocapacitive contributions. The $\text{Nb}_{0.25}\text{Ti}_{0.75}\text{O}_2$ /AC Li-ion hybrid capacitor still showed the highest cell capacitance at the higher scan rate (24.5 F g^{-1} at 100 mV s^{-1} , equivalent to a specific capacity of 14 mAh g^{-1}).

Galvanostatic charge discharge measurements were used to investigate electrochemical performance of the hybrid supercapacitors further. The cell specific capacitance was calculated using equations (2) and (3):

$$C_{\text{cell}} = (I \times t) / (\Delta V \times m), \quad (2)$$

$$\Delta V = E_{\text{max}} - E_{\text{min}}, \quad (3)$$

where I is the charge current in A, t is the discharge time, ΔV is the potential window in V, and m is the mass of active material in both the anode and cathode in grams. E_{max} and E_{min} are the potentials at the beginning and at the end of the discharge cycle. E_{max} therefore decreased with increasing applied current, because increasing current increased the IR drop.

The cells were cycled in the potential window of $0.5\text{--}3.0 \text{ V}$ as well as $1.0\text{--}3.0 \text{ V}$, at current densities in the range $0.5\text{--}50 \text{ mA cm}^{-2}$, equivalent to specific currents in the range of ca. $0.1\text{--}10 \text{ A g}^{-1}$, based on the mass of active material in both cathode and anode. Figures 6(a) and (b) show the charge–discharge profiles at 0.5 , 5 and 10 mA cm^{-2} (equivalent to ca. 0.1 , 1 and 2 A g^{-1}) in the potential window of $0.5\text{--}3.0 \text{ V}$. The curves for all samples deviated from the triangular shape expected for electric double layer capacitors because of the combination of Faradaic and non-Faradaic charge storage mechanisms. As expected from the specific capacitance measurements at high scan rates, $\text{Nb}_{0.25}\text{Ti}_{0.75}\text{O}_2$ /AC hybrid Li-ion capacitors showed the best performance at high current densities. Compared to the other two samples, the equivalent series resistance (and therefore IR drop) was

significantly smaller for this hybrid Li-ion capacitor, potentially because of the lower electronic resistivity in $\text{Nb}_{0.25}\text{Ti}_{0.75}\text{O}_2$ compared to undoped TiO_2 (Lübke *et al* 2015). The specific capacitance for the $\text{Nb}_{0.25}\text{Ti}_{0.75}\text{O}_2$ /AC hybrid supercapacitor was 40 , 39 , and 39 F g^{-1} (equivalent to specific capacities of 28 , 25 , and 23 mAh g^{-1}) at current densities of 0.5 , 5 , and 10 mA cm^{-2} (equivalent to ca. 0.1 , 1 and 2 A g^{-1}), respectively. In comparison, the Mo-doped TiO_2 /AC hybrid Li-ion capacitor showed a high capacitance of 42 F g^{-1} (equivalent to a specific capacity of 30 mAh g^{-1}) at 0.5 mA cm^{-2} , which declined to 21.5 F g^{-1} (equivalent to a specific capacity of 10 mAh g^{-1}) at 10 mA cm^{-2} .

In the narrower potential window of $1.0\text{--}3.0 \text{ V}$, the $\text{Mo}_{0.1}\text{Ti}_{0.9}\text{O}_2$ /AC hybrid supercapacitor retained specific cell capacitances of 35 , 31 , 26 and 21 F g^{-1} (equivalent to specific capacities of 20 , 16 , 12 and 8 mAh g^{-1} , respectively) at current densities of 2 , 5 , 10 and 20 mA cm^{-2} (equivalent to ca. 0.4 , 1 , 2 and 4 A g^{-1}), respectively. The TiO_2 /AC hybrid supercapacitor showed capacitances of 34 , 27 , 22 , and 16 F g^{-1} (18 , 13 , 9 and 5 mAh g^{-1} , respectively) at the corresponding current densities. The charge–discharge curves are shown in figures 6(c) and (d). Coulombic efficiencies for all charge discharge cycles shown in figure 6 are shown in figure S2 (see ESI).

The results of the rate testing for the $\text{Mo}_{0.1}\text{Ti}_{0.9}\text{O}_2$ /AC hybrid Li-ion capacitor are shown in figure 7. At a low current density (2 mA cm^{-2}), a specific capacitance of 37 F g^{-1} was measured after 100 cycles, and even at high current densities of 20 mA cm^{-2} , its specific capacitance was still 22 F g^{-1} (specific capacity of 7 mAh g^{-1}). Coulombic efficiencies were only ca. 99% at 2 mA cm^{-2} , but above 99.5% for all higher current densities, and 100% at 50 mA cm^{-2} . Whilst at lower current densities the $\text{Mo}_{0.1}\text{Ti}_{0.9}\text{O}_2$ /AC hybrid Li-ion capacitor showed lower specific capacitance but better stability than comparable devices, performance at high rate was comparable to a TiO_2 -(reduced graphene oxide)/AC Li-ion hybrid capacitor and better at the highest current density of 50 mA cm^{-2} (Kim *et al* 2013). $\text{Mo}_{0.1}\text{Ti}_{0.9}\text{O}_2$ /AC hybrid Li-ion capacitors showed consistently higher specific capacitance

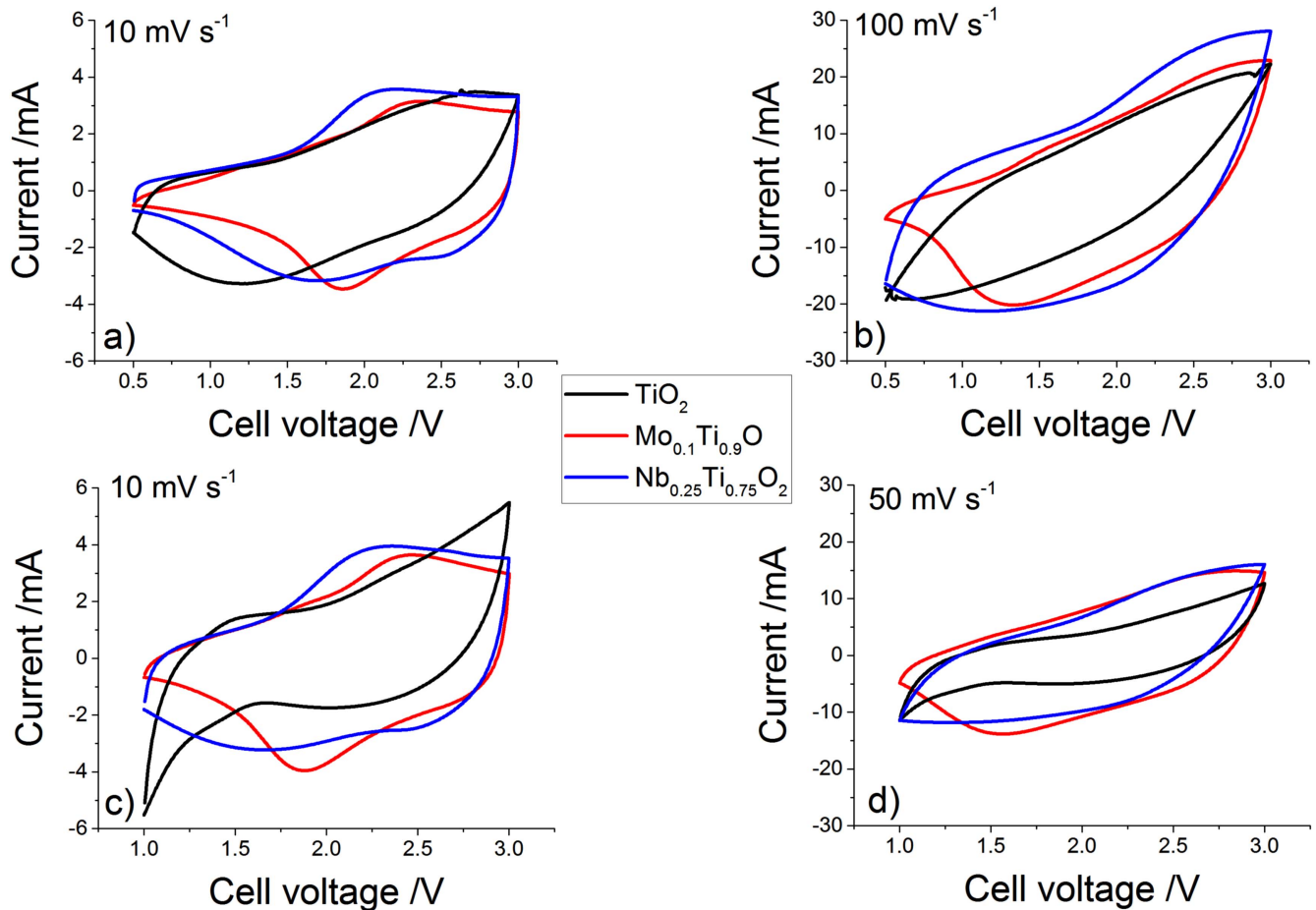


Figure 5. Cyclic voltammetry (CV) analysis of the different hybrid supercapacitors at scan rates of (a) 10 mV s^{-1} and (b) 100 mV s^{-1} when cycled in the potential window 0.5–3.0 V and in the potential window 1.0–3.0 V at scan rates of (c) 10 mV s^{-1} and (d) 50 mV s^{-1} .

than TiO_2/AC capacitors at all current densities (see figures S3(a) and (b)).

Further, the $\text{Mo}_{0.1}\text{Ti}_{0.9}\text{O}_2/\text{AC}$ displayed good cyclability, with good stability at current densities of 2 and 5 mA cm^{-2} (see figure S3(c)), and capacity retention of 75% capacity after 5250 cycles (see figure S4). This was better than comparable devices from the literature using $\text{LiNi}_{0.5}\text{Mn}_{1.5}\text{O}_4$, $\text{Li}_4\text{Ti}_5\text{O}_{12}$ or $\text{TiO}_2\text{-B}$ electrodes and AC cathodes (Aravindan *et al* 2013, Arun *et al* 2015, Dsoke *et al* 2015).

Both energy (E) and power (P) density were calculated using equations (4)–(6) to further investigate the performance:

$$P = \Delta V \times (I/m), \quad (4)$$

$$E = P \times (t/3600), \quad (5)$$

$$\Delta V = (E_{\max} + E_{\min})/2, \quad (6)$$

where E_{\max} and E_{\min} are the potentials at the beginning and the end of the discharge, therefore, ΔV gives the average potential, I is the current in A, m is the mass of the active materials in both anode and cathode (in kg) and t is the discharge time (in seconds). When cycled in the range 0.5 and 3.0 V, the $\text{Mo}_{0.1}\text{Ti}_{0.9}\text{O}_2/\text{AC}$ hybrid supercapacitor delivered the highest observed energy density of 51 Wh kg^{-1} at a power density of 180 W kg^{-1} . However, because of the superior

capacitance retention at higher currents in this potential window, the $\text{Nb}_{0.25}\text{Ti}_{0.75}\text{O}_2/\text{AC}$ hybrid supercapacitor performed better at higher power densities; the cell yielded a specific energy density of 41 Wh kg^{-1} at 1700 W kg^{-1} or conversely an energy density of 36 Wh kg^{-1} at 3200 W kg^{-1} , which is amongst the best performance found in the comparable literature at these high rates.

The narrower potential window of 1.0–3.0 V led to an increased average power. The $\text{Mo}_{0.1}\text{Ti}_{0.9}\text{O}_2/\text{AC}$ hybrid Li-ion capacitor showed high energy retention at high power densities, with an energy density of 29 Wh kg^{-1} at a power density of 2000 W kg^{-1} or 12 Wh kg^{-1} at 6700 W kg^{-1} . Even at 14100 W kg^{-1} , the energy density was still 2.5 Wh kg^{-1} .

To demonstrate the performance of the Li-ion capacitors compared to similar systems in the literature, a Ragone graph was plotted showing the data herein alongside Li-ion capacitors employing different anode materials including TiO_2 -Reduced Graphene oxide (Kim *et al* 2013, 2016) and anatase TiO_2 (Kim *et al* 2013), $\text{Li}_4\text{Ti}_5\text{O}_{12}$ (Ni *et al* 2012, Kim *et al* 2016), $\text{TiO}_2\text{-B}$ (Wang *et al* 2006), $\text{TiO}_2(\text{B})$ (Aravindan *et al* 2013), LiCrTiO_4 (Aravindan *et al* 2012), Ti_9O_{17} (Han and Wang 2010), and TiO_2 microspheres wrapped with graphene nanosheets cycled against a graphene nanosheet positive electrode (Wang *et al* 2016) in figure 8. The plot clearly

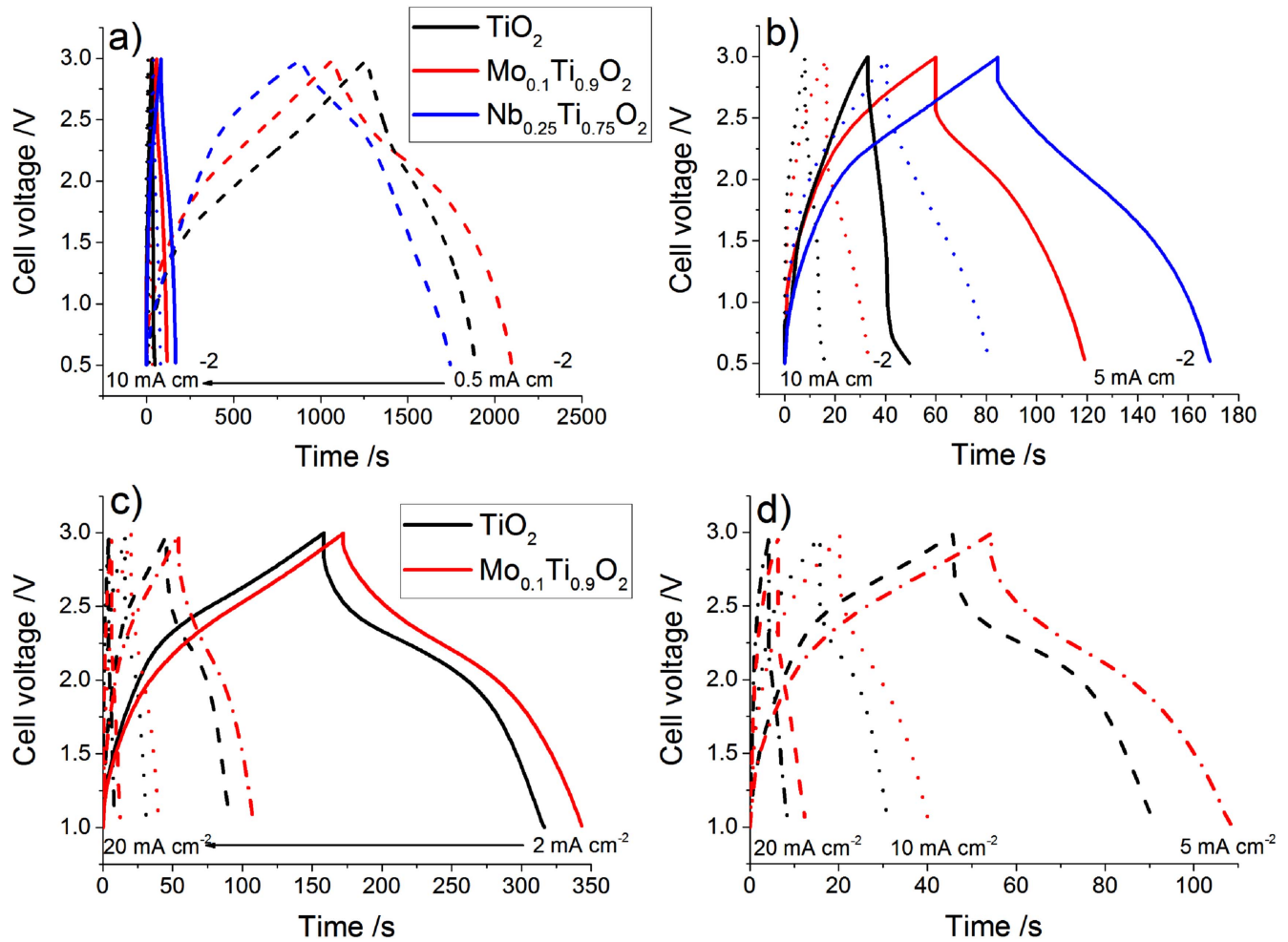


Figure 6. (a) and (b) Charge discharge profiles of the different supercapacitors cycled in the potential window 0.5–3.0 V at different current densities of 0.5 (solid lines), 5 (dashes) and 10 mA cm⁻² (dotted lines). (c) and (d) Charge discharge profiles of the Mo_{0.1}Ti_{0.9}O₂/AC and the TiO₂/AC hybrid supercapacitor cycled in the potential window 1.0–3.0 V at different current densities of 2 (solid lines), 5 (dashes), 10 (dotted lines) and 20 mA cm⁻² (dash-dot).

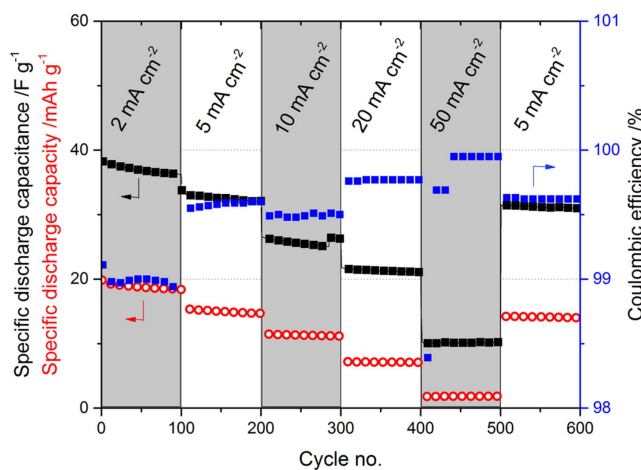


Figure 7. Cycling performance at various current densities for the Mo_{0.1}Ti_{0.9}O₂/AC supercapacitor cycled in the potential window 1.0–3.0 V. The current densities of 2, 5, 10, 20 and 50 mA cm⁻² were equivalent to specific currents of ca. 0.4, 1, 2, 4 and 10 A g⁻¹, respectively, calculated based on the mass of active material in both electrodes.

showed that both Nb-doped and Mo-doped anatase TiO₂ synthesised via CHFS were promising as active anode material of hybrid Li-ion supercapacitors. Among hybrid Li-ion supercapacitors with TiO₂-based anodes and AC positive electrodes, the devices presented herein showed the best performance at various power densities because of the improved pseudocapacitive charge storage at higher rates which was due to doping and high specific surface area of the nanoparticles. When compared to devices with more elaborated anodes (such as microspheres wrapped with graphene nanosheets) and cathodes (graphene nanosheets) (Wang *et al* 2016), the observed energy densities were still better at high power densities.

4. Conclusions

High surface area molybdenum or niobium doped TiO₂ as well as undoped titania were synthesised in a single step process using a continuous hydrothermal flow system. The

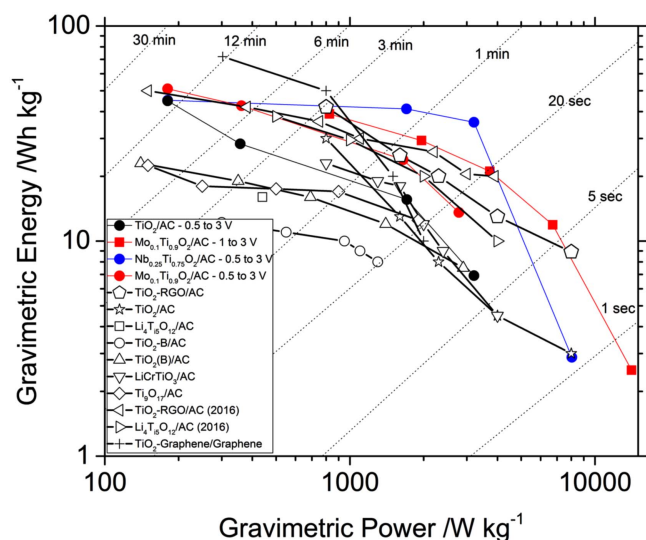


Figure 8. Comparative Ragone plot of the best results from this work (red and blue plots) with similar devices tested in the literature. The supercapacitors the devices were compared to here included ones using anodes such as TiO₂-reduced graphene oxide and anatase TiO₂ (Kim *et al* 2013), Li₄Ti₅O₁₂ (Ni *et al* 2012), TiO₂-B (Wang *et al* 2006), TiO₂(B) (Aravindan *et al* 2013), LiCrTiO₄ (Aravindan *et al* 2012), Ti₉O₁₇ (Han and Wang 2010), TiO₂-reduced graphene oxide (2016) and Li₄Ti₅O₁₂ (2016) (Kim *et al* 2016), TiO₂ microspheres wrapped with graphene nanosheets versus a graphene nanosheet positive electrode (Wang *et al* 2016). Reproduced with permission from the Society of Polymer Science, Japan, copyright 2017.

high surface area as well as the doping of ions with a higher valence state than that of the Ti⁴⁺-ions in titania, improved the (extrinsic) pseudocapacitive (surface-near) charge storage in these materials. Nanomaterials synthesised via such a process were used in supercapacitors for the first time.

Doped TiO₂/AC Li-ion capacitors using organic Li-ion electrolyte showed high energy and high power density, with energy densities of up to 51 Wh kg⁻¹. The most promising results, however, were achieved at medium power densities and energy densities, for example the Nb_{0.25}Ti_{0.75}O₂/AC hybrid supercapacitor achieved 41 Wh kg⁻¹ at 1700 W kg⁻¹ and 36 Wh kg⁻¹ at 3200 W kg⁻¹. Comparison to similar work in the literature showed superior performance compared to other anatase/AC Li-ion capacitor, as well as Li-ion capacitors using more elaborate titanium based active materials.

These results show that nanomaterials synthesised via the scalable CHFS method hold promise for anodes in hybrid supercapacitors because of the increased pseudocapacitive charge storage due to high surface area and doping with metal ions.

Acknowledgments

The EPSRC are thanked for funding the Centre for Doctoral Training in Molecular Modelling & Materials Science (UCL, UK) and JAIST (Kanazawa, Japan) are thanked for supporting a studentship for DB. JAD thanks EPSRC for

support of the ELEVATE (ELeTrochemical Vehicle Advanced Technology) low carbon vehicles project (EP/M009394/1). Dr Chris Tighe and Dr Rob Guar are thanked for their contributions towards development of the current laboratory scale CHFS process, which was used in this work.

References

- Aravindan V *et al* 2013 Constructing high energy density non-aqueous Li-ion capacitors using monoclinic TiO₂-B nanorods as insertion host *J. Mater. Chem. A* **1** 6145–51
- Aravindan V *et al* 2014 Insertion-type electrodes for nonaqueous Li-ion capacitors *Chem. Rev.* **114** 11619–35
- Aravindan V, Chuiling W and Madhavi S 2012 High power lithium-ion hybrid electrochemical capacitors using spinel LiCrTiO₄ as insertion electrode *J. Mater. Chem.* **22** 16026–31
- Arun N *et al* 2015 Nanostructured spinel LiNi_{0.5}Mn_{1.5}O₄ as new insertion anode for advanced Li-ion capacitors with high power capability *Nano Energy* **12** 69–75
- Augustyn V, Simon P and Dunn B 2014 Pseudocapacitive oxide materials for high-rate electrochemical energy storage *Energy Environ. Sci.* **7** 1597–614
- Brezesinski T *et al* 2009 Templated nanocrystal-based porous TiO₂ films for next-generation electrochemical capacitors *J. Am. Chem. Soc.* **131** 1802–9
- Chen M *et al* 2011 Modelling and simulation of continuous hydrothermal flow synthesis process for nano-materials manufacture *J. Supercrit. Fluids* **59** 131–9
- Deng S *et al* 2014 Synthesis and electrochemical properties of Li₄Ti₅O₁₂ spheres and its application for hybrid supercapacitors *Electrochim. Acta* **146** 37–43
- Dsoke S *et al* 2015 The importance of the electrode mass ratio in a Li-ion capacitor based on activated carbon and Li₄Ti₅O₁₂ *J. Power Sources* **282** 385–93
- Dylla A G, Henkelman G and Stevenson K J 2013 Lithium insertion in nanostructured TiO₂(B) architectures *Acc. Chem. Res.* **46** 1104–12
- Guar R I, Tighe C J and Darr J A 2013 Scaling-up a confined jet reactor for the continuous hydrothermal manufacture of nanomaterials *Ind. Eng. Chem. Res.* **52** 5270–81
- Han W-Q and Wang X-L 2010 Carbon-coated Magnéli-phase Ti_nO_{2n-1} nanobelts as anodes for Li-ion batteries and hybrid electrochemical cells *Appl. Phys. Lett.* **97** 2431041–3
- Härmäs M *et al* 2016 Microporous-carbons for energy storage synthesized by activation of carbonaceous material by zinc chloride, potassium hydroxide or mixture of them *J. Power Sources* **326** 624–34
- Hu X *et al* 2015 Nanostructured Mo-based electrode materials for electrochemical energy storage *Chem. Soc. Rev.* **44** 2376–404
- Ibrahim H, Ilinca A and Perron J 2008 Energy storage systems-characteristics and comparisons *Renew. Sustain. Energy Rev.* **12** 1221–50
- Ji W *et al* 2014 Partially nitrated molybdenum trioxide with promoted performance as an anode material for lithium-ion batteries *J. Mater. Chem. A* **2** 699–704
- Kim H *et al* 2013 A novel high-energy hybrid supercapacitor with an anatase TiO₂-reduced graphene oxide anode and an activated carbon cathode *Adv. Energy Mater.* **3** 1500–6
- Kim H K *et al* 2016 TiO₂-reduced graphene oxide nanocomposites by microwave-assisted forced hydrolysis as excellent insertion anode for Li-ion battery and capacitor *J. Power Sources* **327** 171–7

- Lee S H *et al* 2014 A novel high-performance cylindrical hybrid supercapacitor with $\text{Li}_{4-x}\text{Na}_x\text{Ti}_5\text{O}_{12}$ /activated carbon electrodes *Int. J. Hydrog. Energy* **39** 16569–75
- Lee S H *et al* 2015 Novel performance of ultrathin AlPO_4 coated $\text{H}_2\text{Ti}_{12}\text{O}_{25}$ Exceeding $\text{Li}_4\text{Ti}_5\text{O}_{12}$ in cylindrical hybrid supercapacitor *J. Power Sources* **273** 839–43
- Li R *et al* 2015 Carbon-stabilized high-capacity ferromagnetic oxide nanorod array for flexible solid-state alkaline battery-supercapacitor hybrid device with high environmental suitability *Adv. Funct. Mater.* **25** 5384–94
- Li R *et al* 2016 Nanoscale Horizons nanowire arrays for high energy density aqueous asymmetric supercapacitors *Nanoscale Horiz.* **1** 150–5
- Lim E *et al* 2014 Advanced hybrid supercapacitor based on a mesoporous niobium pentoxide/carbon as high-performance anode *ACS Nano* **8** 8968–78
- Liu H *et al* 2011 Mesoporous TiO_2 -B microspheres with superior rate performance for lithium ion batteries *Adv. Mater.* **23** 3450–4
- Lübke M *et al* 2015 Highly pseudocapacitive Nb-doped TiO_2 high power anodes for lithium-ion batteries *J. Mater. Chem. A* **3** 22908–14
- Lust *et al* 2002 Electrochemical properties of nanoporous carbon electrodes *Condens. Matter Phys.* **5** 307
- Naoi K *et al* 2010 High-rate nano-crystalline $\text{Li}_4\text{Ti}_5\text{O}_{12}$ attached on carbon nano-fibers for hybrid supercapacitors *J. Power Sources* **195** 6250–4
- Ni J *et al* 2012 A high-performance hybrid supercapacitor with $\text{Li}_4\text{Ti}_5\text{O}_{12}$ -C nano-composite prepared by *in situ* and *ex situ* carbon modification *J. Solid State Electrochem.* **16** 2791–6
- Palacín M R 2009 Recent advances in rechargeable battery materials: a chemist's perspective *Chem. Soc. Rev.* **38** 2565–75
- Plitz I *et al* 2006 The design of alternative nonaqueous high power chemistries *Appl. Phys. A* **82** 615–26
- Stoller M D *et al* 2011 Interfacial capacitance of single layer graphene *Energy Environ. Sci.* **4** 4685
- Thi T V *et al* 2014 Effect of Mo^{6+} doping on electrochemical performance of anatase TiO_2 as a high performance anode material for secondary lithium-ion batteries *J. Alloys Compd.* **598** 16–22
- Tighe C J *et al* 2013 Scale up production of nanoparticles: continuous supercritical water synthesis of Ce–Zn oxides *Ind. Eng. Chem. Res.* **52** 5522–8
- Wang F *et al* 2016 A quasi-solid-state Li-ion capacitor based on porous TiO_2 hollow microspheres wrapped with graphene nanosheets *Small* **12** 6207–13
- Wang J *et al* 2007 Pseudocapacitive contributions to electrochemical energy storage in TiO_2 (anatase) nanoparticles *J. Phys. Chem. C* **111** 14925–31
- Wang Q, Wen Z and Li J 2006 A hybrid supercapacitor fabricated with a carbon nanotube cathode and a TiO_2 -B nanowire anode *Adv. Funct. Mater.* **16** 2141–6
- Xia X *et al* 2015 VO_2 nanoflake arrays for supercapacitor and Li-ion battery electrodes: performance enhancement by hydrogen molybdenum bronze as an efficient shell material *Mater. Horiz.* **2** 237–44
- Yang Z *et al* 2009 Nanostructures and lithium electrochemical reactivity of lithium titanates and titanium oxides: a review *J. Power Sources* **192** 588–98
- Zhang J *et al* 2014 Molybdenum-doped titanium dioxide and its superior lithium storage performance *J. Phys. Chem. C* **118** 25300–9
- Zuo W *et al* 2015 Directly grown nanostructured electrodes for high volumetric energy density binder-free hybrid supercapacitors: a case study of CNTs// $\text{Li}_4\text{Ti}_5\text{O}_{12}$ *Sci. Rep.* **5** 7780
- Zuo W *et al* 2017 Battery-supercapacitor hybrid devices: recent progress and future prospects *Adv. Sci.* **1600539**